research papers

Symmetry-mode analysis for intuitive observation of structure–property relationships in the lead-free antiferroelectric (1−x)AgNbO₃–xLiTaO₃

Teng Lu,[a]‡ Ye Tian,[b,a,c]*‡ Andrew Studer,[d] Narendirakumar Narayanan,[a,d] Qian Li,[e] Ray Withers,[a] Li Jin,[b] Y. Mendez-González,[f] A. Peláiz-Barranco,[f] Dehong Yu,[d] Garry J. McIntyre,[d] Zhuo Xu,[b] Xiaoyong Wei,[b]* Haixue Yan[c] and Yun Liu[a]*

[a]Research School of Chemistry, Australian National University, Canberra, ACT 2601, Australia, [b]Electronic Materials Research Laboratory, Xi'an Jiaotong University, Xi'an, Shannxi 710049, People's Republic of China, [c]School of Engineering and Materials Science, Queen Mary University of London, London E1 4NS, UK, [d]Australian Nuclear Science and Technology Organisation, New Illawarra Road, Lucas Heights, NSW 2234, Australia, [e]Advanced Photon Source, Argonne National Laboratory, Argonne, IL 60439, USA, and [f]Physics Faculty, Institute of Science and Technology of Materials, Havana University, Cuba. *Correspondence e-mail: y.tian@mail.xjtu.edu.cn, wdy@xjtu.edu.cn, yun.liu@anu.edu.au

Functional materials are of critical importance to electronic and smart devices. A deep understanding of the structure–property relationship is essential for designing new materials. In this work, instead of utilizing conventional atomic coordinates, a symmetry-mode approach is successfully used to conduct structure refinement of the neutron powder diffraction data of $(1-x)$AgNbO₃–xLiTaO₃ ($0 \leq x \leq 0.09$) ceramics. This provides rich structural information that not only clarifies the controversial symmetry assigned to pure AgNbO₃ but also explains well the detailed structural evolution of $(1-x)$AgNbO₃–xLiTaO₃ ($0 \leq x \leq 0.09$) ceramics, and builds a comprehensive and straightforward relationship between structural distortion and electrical properties. It is concluded that there are four relatively large-amplitude major modes that dominate the distorted $Pmc2_1$ structure of pure AgNbO₃, namely a $\Lambda 3$ antiferroelectric mode, a T4+ $a^-a^-c^0$ octahedral tilting mode, an H2 $a^0a^0c^+/a^0a^0c^-$ octahedral tilting mode and a $\Gamma 4-$ ferroelectric mode. The H2 and $\Lambda 3$ modes become progressively inactive with increasing x and their destabilization is the driving force behind the composition-driven phase transition between the $Pmc2_1$ and $R3c$ phases. This structural variation is consistent with the trend observed in the measured temperature-dependent dielectric properties and polarization–electric field (P-E) hysteresis loops. The mode crystallography applied in this study provides a strategy for optimizing related properties by tuning the amplitudes of the corresponding modes in these novel AgNbO₃-based (anti)ferroelectric materials.

1. Introduction

Functional materials with (anti)ferroelectricity (AFE/FE) offer innumerable applications for sensors, actuators, memory and energy-storage devices (Liu *et al.*, 2015; Hao *et al.*, 2009; Setter *et al.*, 2006; Haertling, 1999; Damjanovic, 1998). Lead-containing materials such as Pb(Zr,Ti)O₃, Pb(Zr,Sn,Ti)O₃ and Pb(Mg₁/₂Nb₂/₃)O₃–PbTiO₃ have already been manufactured into commercial devices due to their excellent properties (Park & Shrout, 1997; Bellaiche & Vanderbilt, 1999; Guo *et al.*, 2000; Mirshekarloo *et al.*, 2010), but environmental concerns nowadays prompt investigations into lead-free alternatives (Saito *et al.*, 2004; Shrout & Zhang, 2007). Recently, AgNbO₃ (AN) has attracted researchers' attention as a novel lead-free AFE material. It is reported that the recoverable energy density of pure AN ceramics can reach 2.1 J cm⁻³. After
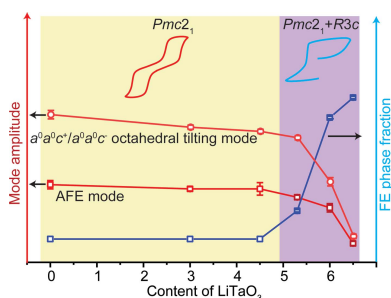
substituting 20% Nb^{5+} with Ta^{5+}, however, the recoverable energy density doubles to ∼4.2 J cm^{-3}, the highest value achieved to date in lead-free AFE ceramics (Zhao *et al.*, 2017; Tian *et al.*, 2016). One of the important reasons enabling such a high energy density in AN is its ultrahigh field-induced polarization (∼52 μC cm^{-2}), which strongly suggests that AN should remain as the basis material from which to develop lead-free alternatives with high piezoelectric performance (Fu *et al.*, 2007, 2008, 2009, 2011*a*). Referring to the investigation carried out by Fu *et al.* (2008), Li$^+$ doping can stabilize the ferroelectricity of AN. More importantly, the synthesized single-crystalline $(Ag_{0.914}Li_{0.086})NbO_3$ exhibits a relatively large piezoelectric coefficient with a higher Curie temperature (T_C), making it a competitive candidate for new lead-free piezoelectrics.

Currently, a considerable amount of effort, especially into chemical modification, is being made to improve the energy storage and/or piezoelectric capabilities of AN-based systems (Tian *et al.*, 2017; Zhao *et al.*, 2018, 2016). Nonetheless, the underlying structure and structural evolution of such doped materials still remain ambiguous and controversial. From a structural point of view, many room-temperature FE and/or AFE structures exhibit at least one large-amplitude (primary) distortive mode, in addition to the fundamental FE (polar $\mathbf{q} = 0$ mode) and/or AFE modes which are directly responsible for their FE and/or AFE properties, when compared with their typically higher-symmetry paraelectric phases (Dove, 1997; Stokes *et al.*, 1991). The traditional single soft-mode approach is unable to describe the complete structural distortion in such circumstances. In seeking to understand the competing structural instabilities underlying the behaviour of such FE and AFE phases, it is thus very useful to utilize a mode crystallography approach, whereby the primary and induced secondary modes of distortion are clearly identified via symmetry-mode decomposition (Perez-Mato *et al.*, 2010). In such an approach, the room-temperature structure is described in terms of an undistorted parent structure and various additional distortive modes. Each mode is then associated with a specific allowed modulation wavevector and irreducible representation (irrep), as well as the mode amplitude.

This work therefore introduces this methodology into the structure refinement of neutron diffraction data collected from pure AN and associated compounds for better understanding of the chemically induced structural evolution and property changes, and is laid out in three parts. In the first part, symmetry-mode decomposition is successfully applied to pure AN for both the non-polar *Pbcm* and polar *Pmc*2$_1$ space groups. It provides new insight into these two controversial symmetries, the origin of which will be addressed below, in terms of distortive modes. In the second part we extend the application of symmetry-mode analysis to the newly synthesized $(1-x)AgNbO_3$–$xLiTaO_3$ material system (ANLT100x hereafter) to build a more precise correlation between the structure and electrical properties of the ANLT system. The latter are presented in the third part. The symmetry-mode decomposition approach shows the variation in the relative amplitudes of the different modes as a function of the LiTaO$_3$ dopant level, thereby enabling a better understanding of the structure of AN itself and its phase-transition behaviour under chemical modification, by comparison with conventional Rietveld fractional coordinate refinements. We believe this work not only presents a systematic investigation of a new AN-based solid-solution system, but also illustrates the influence of composition on the distortive-mode amplitudes and thus on the relative properties. Such an approach can guide future work in enhancing the AFE or FE properties of AN-based materials.

2. Results and discussion

2.1. Symmetry-mode decomposition of AgNbO₃

The average structure of AN at room temperature still remains controversial because either the *Pbcm* or the *Pmc*2$_1$ space group can be used reasonably well for structure refinement based on X-ray and neutron powder diffraction data (Sciau *et al.*, 2004; Levin *et al.*, 2009; Yashima *et al.*, 2011). In this current work, the symmetry-mode decomposition approach is thus adopted to describe obvious differences between these two distorted structures proposed by Levin *et al.* (2009) and Yashima *et al.* (2011), respectively, to reveal a 'hidden structural correlation'. Note that the *Pbcm* and *Pmc*2$_1$ structures use different axes settings. In order to make them comparable and decomposed from the same parent structure, the *Pbcm* structure is transferred into a *Pmca* structure, based on the settings used by Yashima *et al.* (2011). The parent structure was then chosen as an undistorted *Ammm* structure (Fig. 1), which accommodates the octahedral rotation and avoids lattice strain. The unit-cell axes relationship between this *Ammm* structure (subscript A) and the pseudo-cubic perovskite structure with $Pm\overline{3}m$ symmetry (subscript p) is $\mathbf{c}_p \equiv \mathbf{a}_A$, $\mathbf{a}_p + \mathbf{b}_p \equiv \mathbf{b}_A$, $-\mathbf{a}_p + \mathbf{b}_p \equiv \mathbf{c}_A$.

Atomic displacements from the mode decomposition of the distorted *Pmca* and *Pmc*2$_1$ structures are listed in the supporting information (Tables S1 and S2). The *Pmca* structure is the result of irrep distortions of the *Ammm* parent structure associated with five different irrep modes: Λ3, Y3−, Z2−, T4+ and H2. However, the associated atomic displacements for different modes display strong differences. Taking
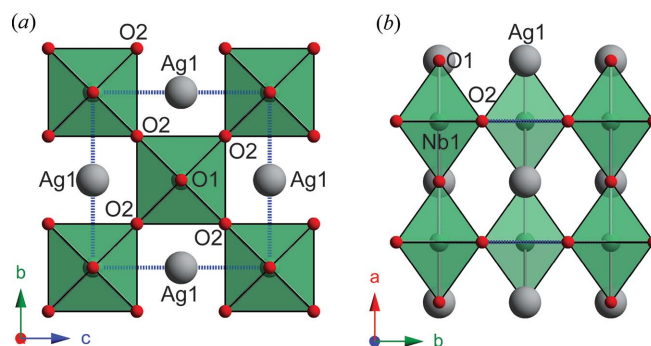
Figure 1
The parent *Ammm* structure viewed along (*a*) the *a* axis and (*b*) the *c* axis.

Table 1
The dimensions and global amplitudes of distortive modes observed in the *Pmca* and *Pmc*2$_1$ structures.

The **q** vector basis refers to the *Ammm* and pseudo-cubic perovskite structures.

Wavevector **q**				Dimension		A_τ (Å)	
Ammm	Pseudo-cubic	q_i	Irrep	*Pmca*	*Pmc*2$_1$	*Pmca*	*Pmc*2$_1$
[0 0 0]*	[0 0 0]$_p$*	q_0	Γ4−		5		0.21
[1/4 0 0]*	[0 0 1/4]$_p$*	q_1	Λ1		4		0.09
[1/4 0 0]*	[0 0 1/4]$_p$*	q_2	Λ3	5	5	0.48	0.47
[0 1 0]*	[1/2 1/2 0]$_p$*	q_3	Y2+		2		0.17
[0 1 0]*	[1/2 1/2 0]$_p$*	q_4	Y3−	3	3	0.16	0.16
[1/2 0 0]*	[0 0 1/2]$_p$*	q_5	Z3+		2		0.03
[1/2 0 0]*	[0 0 1/2]$_p$*	q_6	Z2−	2	2	0.04	0.02
[1/2 1 0]*	[1/2 1/2 1/2]$_p$*	q_7	T4+	3	3	1.23	1.22
[1/4 1 0]*	[1/2 1/2 1/4]$_p$*	q_8	H2	2	2	1.00	0.97
[1/4 1 0]*	[1/2 1/2 1/4]$_p$*	q_9	H4		4		0.11

O3 as an example, the shift associated with the T4+ mode along the *a* axis is around 0.217 Å, while the shift resulting from the Z2− mode is only 0.004 Å, smaller than the standard deviation for the refinement. For the polar *Pmc*2$_1$ structure, the origin is allowed to shift along the *c* direction. In this case, five more modes are allowed by comparison with the *Pmca* structure (Table S2), which are Γ4−, Λ1, Y2+, Z3+ and H4. Similarly, the atomic displacements associated with modes like Λ1 and Z2− are much smaller than the associated standard deviation. For each individual mode, the dimensions indicate the number of independent components or basis modes involved, and are larger for *Pmc*2$_1$ (32) than for *Pmca* (15).

The global amplitude, A_τ, is calculated by $(\Sigma_m A_{\tau,m}^2)^{1/2}$, where $A_{\tau,m}$ denotes the amplitude for the specific component *m*. The dimensions and global amplitudes for each mode are listed together with the corresponding wavevectors **q** in Table 1 for both distorted structures. Clearly, the T4+, H2 and Λ3 modes have significantly larger global amplitudes in both cases. In the following, we identify the irrep modes whose condensation leads directly to the observed distortions. Referring to the 'isotropy' subgroups (Campbell *et al.*, 2006), the primary modes usually have the larger amplitudes. For *Pmca* symmetry, any two of the Λ3, T4+ and H2 modes could result in the observed distortions. Taking the relative amplitudes into consideration, we identify T4+ and H2 as the most important primary modes. Referring to the wavevectors listed in Table 1, the Λ3 mode can therefore be assigned to a secondary mode induced by the two most important co-existing primary T4+ and H2 modes, *i.e.* $q_2 = q_7 − q_8$. However, for the lowering of the symmetry to *Pmc*2$_1$, the condensation of the T4+ and H2 modes is insufficient. To obtain this structure another primary mode is required, namely the Γ4− mode at the zone centre with a relatively large amplitude. The *Pmc*2$_1$ structure can then be considered as a subgroup of the *Pmca* structure. Therefore, we will focus on the four main modes T4+, H2, Λ3 and Γ4− step by step to understand the structural origin of the properties observed in silver niobate.

Figs. 2(*a*) and 2(*b*) show the distorted AN structure induced by the addition of the T4+ mode only to the *Ammm* parent

structure. This $q_7 = [1/2\ 1\ 0]$* T point mode occurs at the first Brillouin-zone boundary of its parent *Ammm* structure. The displacements involved correspond to a pure $R(\langle 110 \rangle_p)$-type octahedral rotation around the $\mathbf{c} = \mathbf{c}_A \equiv -\mathbf{a}_p + \mathbf{b}_p$ axis, *i.e.* $a^-a^-c^0$ octahedral tilting in Glazer notation (Glazer, 1975). Figs. 2(*c*) and 2(*d*) show the distorted structure induced by the $q_8 = [1/4\ 1\ 0]$ (equivalent to [1/2 1/2 1/4]$_p$*) H2 mode, which also occurs at the Brillouin-zone boundary and is also associated with octahedral rotation, but this time around the $\mathbf{a} = 4\mathbf{a}_A = 4\mathbf{c}_p$ axis. The H2 mode thus exhibits $R(\langle 001 \rangle_p)$-type octahedral rotation, *i.e.* rotation around the **a** axis, but not in the usual in-phase or antiphase rotation patterns expected for perovskites. If the structure is viewed along **a** [Fig. 2(*c*)], it can be seen that the NbO$_6$ octahedra are antiphase tilted. In fact, this is because the adjacent NbO$_6$ octahedra rotate alternately in a single column along the *a* axis [Fig. 2(*d*)]. If the '+' sign denotes that the octahedron rotates clockwise and the '−' sign denotes anticlockwise rotation viewed along **a**, the NbO$_6$ octahedra [the right-hand column in Fig. 2(*d*)] rotate in the form of − − + + − − around the *a* axis, or $a^0a^0c^+/a^0a^0c^-$. In other words, if the adjacent octahedra with in-phase tilt are regarded together as one unit, the dashed red lines in Fig. 2(*d*) can be considered as antiphase boundaries between these units. When combined with the T4+ mode, the resultant distorted structure is an $a^-a^-c^+/a^-a^-c^-$ tilting system, close to the reported $a^-b^-c^+/a^-b^-c^-$. In fact, Yashima *et al.* (2011) suggested equal tilting angles along [100]$_p$ and [010]$_p$, *i.e.* $a^-b^-c^+/a^-b^-c^- = a^-a^-c^+/a^-a^-c^-$.

The T4+ and H2 modes together construct the overall octahedral tilting system in AN. It is worth noting that the octahedral tilting involves oxygen displacements and the
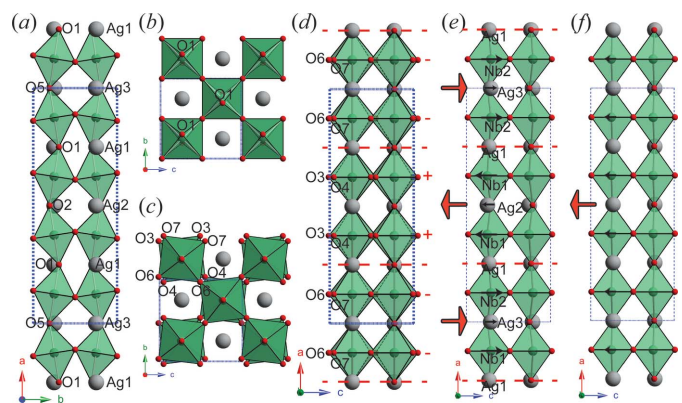

Figure 2
(*a*), (*b*) The distorted AN structure induced by the T4+ mode only, viewed along (*a*) the *c* axis and (*b*) the *a* axis. (*c*), (*d*) The distorted AN structure induced by the H2 mode only, viewed along (*c*) the *a* axis and (*d*) the *b* axis. The +/− signs on the right in panel (*d*) show the clockwise/anticlockwise rotation, respectively, of the right-hand column of octahedra around the *a* axis. (*e*) The distorted structure induced by the Λ3 mode only, and (*f*) that of the Γ4− mode only. The black arrows in panel (*e*) show the off-centre Nb^{5+} and Ag$^+$ cation displacements, while the red arrows in panels (*e*) and (*f*) indicate the local spontaneous polarization. The horizontal dashed red lines represent antiphase boundaries for octahedral rotation around the *a* axis in panel (*d*) and cation displacements along the *c* axis in panel (*e*).

mode amplitude is given in ångströms. The larger amplitude corresponds to a larger distortion. Furthermore, we will also include the tilting angles separately from the mode amplitude to describe the octahedral tilting fully. As mentioned above, the primary T4+ and H2 modes can directly produce a resultant *Pmca* structure.

The distortive structure induced by the next-strongest (induced secondary) $\Lambda 3$ mode is shown in Fig. 2(e) and is mainly related to cation atomic displacements. Within one unit [two octahedral layers thick, shown between two dashed red lines in Fig. 2(e)], the Nb2 and Ag3 atoms are displaced off-centre along **c** [as shown by the black arrows in Fig. 2(e)], while anions such as O6, O7 and O5 are displaced to a lesser extent in the opposite direction. In this two-layer unit, the displaced ions would generate spontaneous polarization along +**c**, as shown by the red arrow. In the adjacent two-layer unit along **a**, cations such as Nb1 and Ag2 are displaced along −**c**, while O2, O3 and O4 again move in the opposite direction, forming an overall dipole moment along −**c**. Note that the Ag1 and O1 ions are located at the boundary between adjacent two-layer units and are thus not allowed to move along the *c* axis as a consequence of a required symmetry operation. Note that the dipole moment formed within each unit has the same magnitude, but the direction switches 180° from one unit to the next, resulting in an antiparallel dipole alignment. In other words, the $\Lambda 3$ mode contributes directly to the observed antiferroelectricity in AN. Intriguingly, the two-layer units drawn in Figs. 2(d) and 2(e) show the same behaviour. After crossing each antiphase boundary, both the octahedral rotation around the *a* axis [in the case of Fig. 2(d)] and the dipole moment [in the case of Fig. 2(e)] change their sign. Considering $\Lambda 3$ as an induced mode, it is evident that the antiferroelectric alignment in AN is very closely related to the observed $a^0a^0c^+/a^0a^0c^-$ (or ++−−) octahedral rotation pattern.

Finally, the distortive structure associated with the zone-centre $\Gamma 4-$ mode only, which, as a primary mode, differentiates the *Pmc2$_1$* structure from the *Pmca* structure by an additional 'softening', is shown in Fig. 2(f). For this ferroelectric **q** = 0 distorted structure, all ions move along the −**c** direction but with different magnitudes. For the cations, the displacements of Ag1, Ag2 and Ag3 (0.002 Å) are much smaller than those of Nb1 and Nb2 (0.059 Å). For the anions, the apical oxygens, *i.e.* O1, O2 and O5, are displaced by 0.025 Å, while the equatorial O3, O4, O6 and O7 anions are displaced by 0.027 Å. As a result, the spontaneous polarization points along −**c**. This $\Gamma 4-$ mode is therefore the origin of the weak ferroelectricity previously observed in silver niobate under a low electric field (*E* field) (Fu *et al.*, 2007). Undoubtedly, both the AFE $\Lambda 3$ mode and the FE $\Gamma 4-$ mode respond to an externally applied *E* field, but the global amplitude of the FE mode is less than half that of the AFE mode. The competition between these two modes thus results in the observed 'ferrielectricity' (Yashima *et al.*, 2011), and also explains the appearance of a non-zero remnant polarization (P_r) observed in the double *P-E* hysteresis loop of AN.

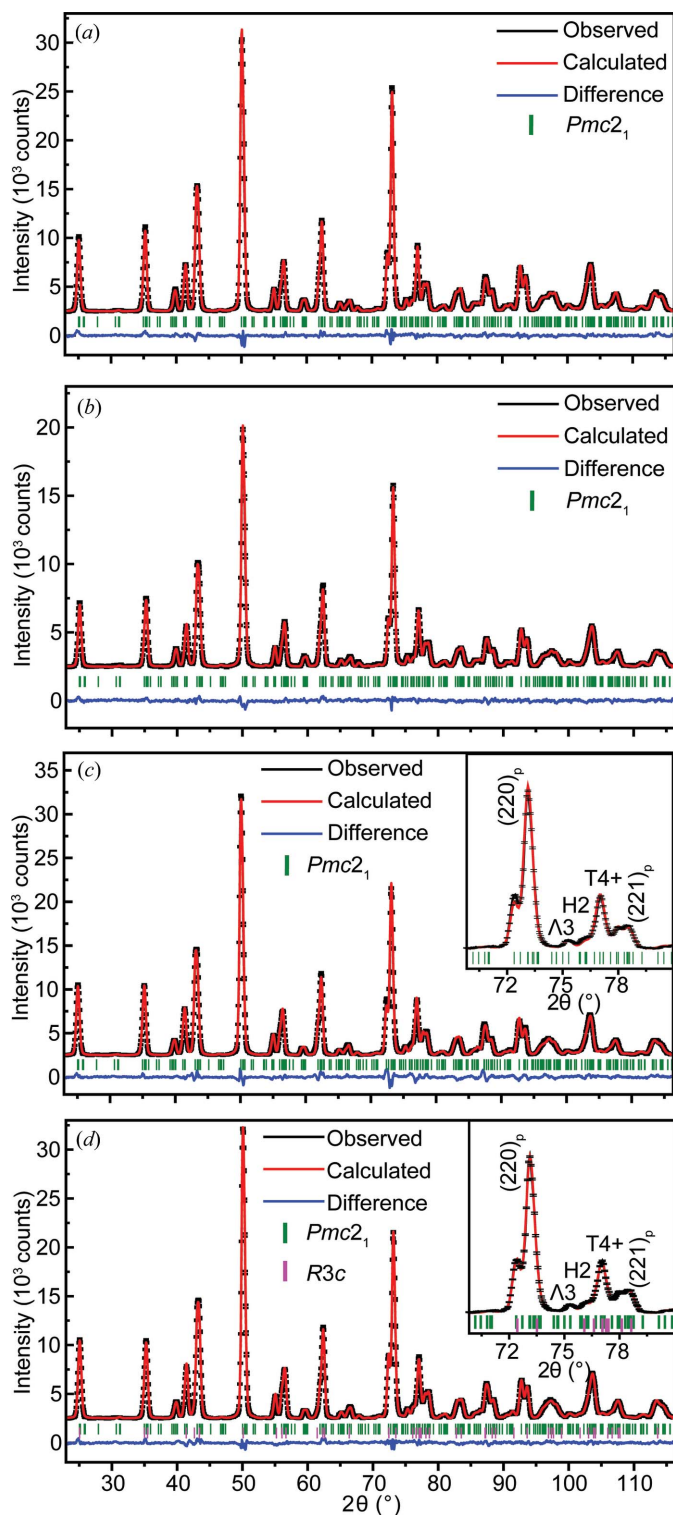## 2.2. Symmetry-mode refinement

In the previous section, we gave a detailed description of the condensation of the various symmetry modes, resulting in the two different space groups and structures reported for AN. In this section, we apply the above relationships to the ANLT100x series of samples for a systematic study of the variation in the modes by a mode-refinement procedure, which was conducted using the *FULLPROF* suite (Rodríguez-Carvajal, 1993) in conjunction with *ISODISTORT* (Campbell *et al.*, 2006). In contrast with conventional Rietveld refinement, the refinement of distortive modes enables a reasonable approach to refining the distorted structures, *e.g.* the primary modes should be refined first and modes with large amplitudes given higher priority. The reference structure was chosen to be the distorted perovskite-type structure with *Pmc2$_1$* space-group symmetry. This is due to the fact that both convergent-beam electron diffraction (CBED) and selected-area electron diffraction (SAED) prove the existence of a polar structure on the local scale (Tian *et al.*, 2016; Yashima *et al.*, 2011). Furthermore, as described in the previous section, the *Pmc2$_1$* structure exhibits an additional primary mode, the $\Gamma 4-$ mode, which explains the observed weak ferroelectricity in a low *E* field. It is thus more reasonable to investigate its variation as a function of LiTaO$_3$ content. A systematic correlation of this mode with the ferroic properties may solve the apparent puzzle regarding the room-temperature AN structure.

Fig. 3(a) shows the neutron powder diffraction (NPD) data of pure AN collected in the 2θ range of 22–116°, while Figs. 3(b) and 3(c) show selected reflections associated with the T4+, H2 and $\Lambda 3$ modes. It is clear that the symmetry-mode refinement approach provides detailed information about the reflection intensities associated with the different modes. For example, the reflections around 2θ = 41.5 and 55° are induced by the T4+ mode, related to the antiphase NbO$_6$ octahedral rotation around [110]$_p$. Additionally, the reflections around 39.8 and 59.5° can be attributed to the combination of the $\Lambda 3$ and H2 modes, with their intensities mainly determined by the H2 mode as a result of its larger global amplitude.

The *Pmc2$_1$* single-phase model was also attempted on NPD patterns of other ANLT100x samples. Given the relatively low
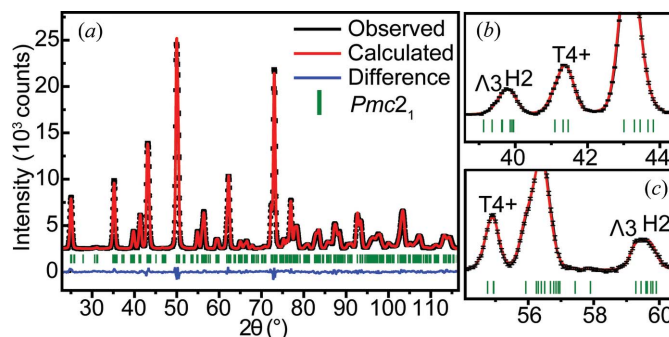
Figure 3
(a) Rietveld symmetry-mode refinement based on the *Pmc2$_1$* space group with the neutron powder diffraction (NPD) data of AN at room temperature. (b), (c) Selected reflections associated with the T4+, H2 and $\Lambda 3$ modes.

Teng Lu *et al.* · Symmetry-mode analysis of $(1-x)$AgNbO$_3$–xLiTaO$_3$

Figure 4
Rietveld symmetry-mode refinement of the NPD data of ANLT100x, (a) $x = 0.03$, (b) $x = 0.045$ and (c) $x = 0.053$ with a space group of $Pmc2_1$, collected at room temperature. (d) Rietveld symmetry-mode refinement of the NPD pattern of ANLT5.3 in terms of the two-phase model ($R3c$ + $Pmc2_1$). The insert plots in panels (c) and (d) are enlargements of selected reflections, indexed by the related irrep modes.

doping level (<10%), the Li$^+$ and Ta^{5+} ions are fixed at the same positions of Ag$^+$ and Nb^{5+}, respectively. For samples with relatively small x values, e.g. $x = 0.03$ and 0.045, the $Pmc2_1$

single-phase model leads to a reasonable refinement result [Figs. 4(a) and 4(b)]. However, for $x = 0.053$, the $Pmc2_1$ single-phase model fails to fit the experimental data well [Fig. 4(c)] and a large divergence is especially observed in the 2θ range of 70 to 80°. The insert plot indicates that the selected peaks are poorly fitted. Referring to the pseudo-cubic perovskite structure (subscript p), it is found that the largest difference appears in calculating parent reflections such as $\langle 220 \rangle_p^*$ and $\langle 221 \rangle_p^*$. For example, the intensity ratio of the split $[220]_p^*/[202]_p^*$ reflections is incorrectly estimated. Furthermore, the intensity of the $1/2\langle 531 \rangle_p^*$ reflection, determined by the amplitude of the T4+ mode, is underestimated. Interestingly, the calculated intensities of reflections associated with the Λ3 and H2 modes are in good agreement with the experimental data.

A bond-valence sum (BVS) calculation (Brown, 1981) suggests that the substitution of Ta^{5+} for Nb^{5+} does not make a big difference, but the replacement of an Li$^+$ ion for an Ag$^+$ ion would strongly destabilize the parent AN structure. Previous studies of Li-doped AgNbO$_3$ systems (Fu et al., 2008, 2011b; Khan et al., 2012) also reported that, with higher Li$^+$ content, the average structure is transformed into a rhombo-hedral phase and the properties change accordingly. Intuitively, the features of the underestimated reflections in Fig. 4(c) are consistent with the patterns induced by the presence of an $R3c$ symmetry structure. A two-phase model refinement (space groups $Pmc2_1$ and $R3c$) was thus applied to the ANLT5.3 pattern, which evidently improved the refinement quality [Fig. 4(d)].

For the $R3c$ phase, the symmetry-mode decomposition has been done with reference to the reported high-temperature cubic structure of AN [$Pm\bar{3}m$ symmetry, ICSD (Inorganic Crystal Structure Database, http://www2.fiz-karlsruhe.de/icsd_home.html) refcode 55649] (Sciau et al., 2004). The basis of this distorted structure is set as: $\mathbf{a}_r \equiv \mathbf{a}_p + \mathbf{c}_p$, $\mathbf{b}_r \equiv \mathbf{b}_p - \mathbf{c}_p$ and $\mathbf{c}_r \equiv -2\mathbf{a}_p + 2\mathbf{b}_p + 2\mathbf{c}_p$. For the $R3c$ structure, condensation of two primary modes with large amplitudes, namely Γ4− $\mathbf{q}_{r0}$ = $[0\ 0\ 0]_p^*$ and R4+ $\mathbf{q}_{r1}$ = $[1/2\ 1/2\ 1/2]_p^*$, will lead to the observed distortions. The Γ4− $\mathbf{q}_{r0}$ = $[0\ 0\ 0]_p^*$ mode, which allows off-centre ionic shifts along the c axis (the $[111]_p$ direction), contributes to the FE spontaneous polarization. The R4+ $\mathbf{q}_{r1}$ = $[1/2\ 1/2\ 1/2]_p^*$ mode, on the other hand, is associated with antiphase octahedral rotation around the $[111]_p$ direction, i.e. $a^-a^-a^-$ octahedral tilting in Glazer notation (Glazer, 1975).
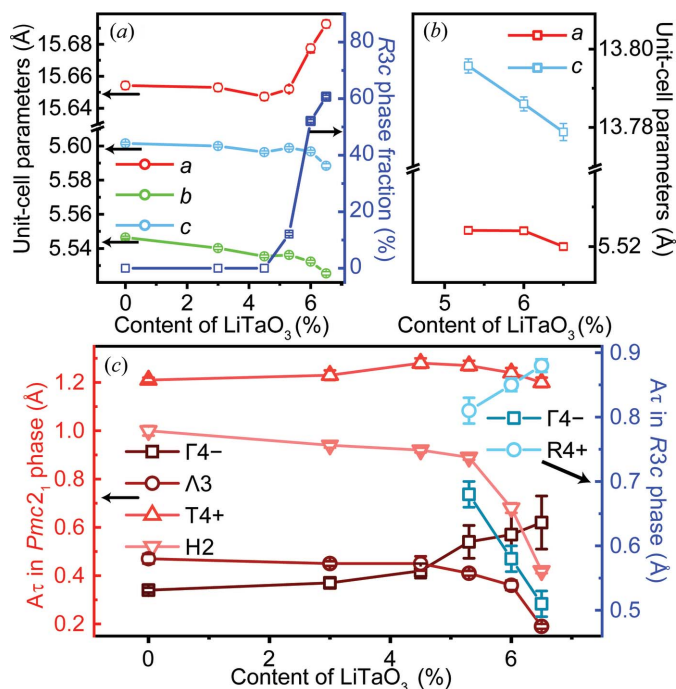
With further doping of LiTaO$_3$, i.e. $x = 0.06$ and 0.09, the features associated with the $R3c$ phase become more obvious. As shown in Fig. 5(a), the $\langle 111 \rangle_p^*$ reflections contain a small shoulder at the lower 2θ angle which does not belong to the $Pmc2_1$ phase. The two-phase model was also applied to refine the data of both ANLT6 and ANLT9 (Fig. 5), resulting in good agreement between the observed and calculated patterns. It should be noted that both the T4+ mode for the $Pmc2_1$ phase and the R4+ mode for the $R3c$ phase contribute to the intensities of the $\mathbf{G}_p \pm [1/2\ 1/2\ 1/2]_p^*$ reflections, so both irrep notations are labelled. For $x = 0.09$, an additional peak observed at 26° [Fig. 5(b), labelled by the red rectangular symbol] is probably from an impure LiNbO$_3$ phase as
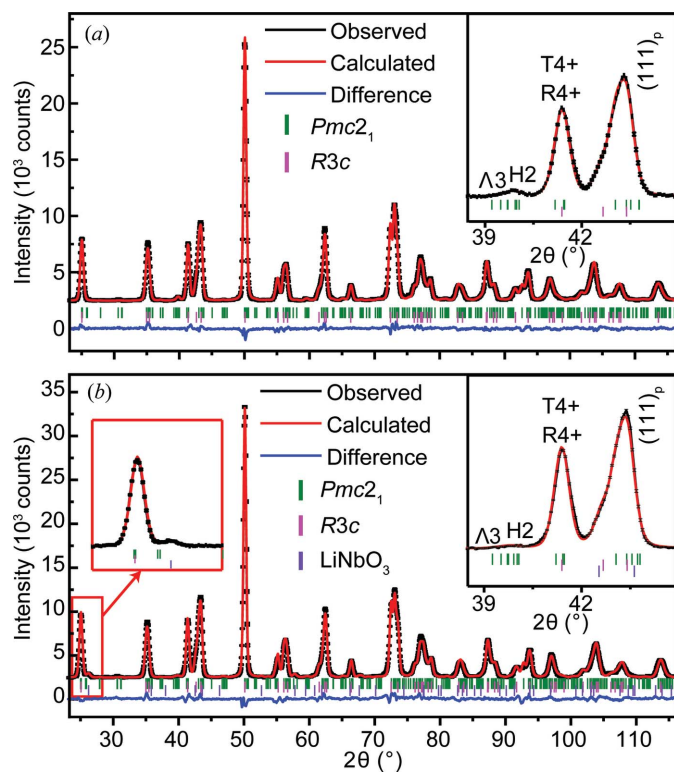
Figure 5
Plots of NPD data with Rietveld analysis for (a) ANLT6 and (b) ANLT9. The insert plots at the top right are enlargements of selected regions. The insert plot with a red frame on the left of panel (b) is an enlargement showing the presence of an impure $LiNbO_3$ phase.
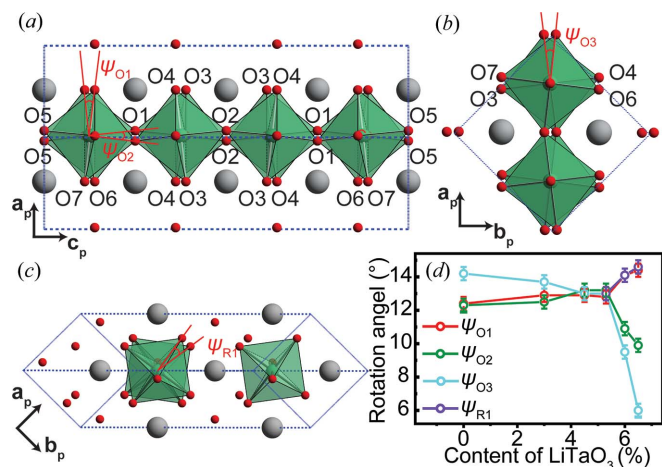

Figure 6
(a) Refined lattice parameters of the $Pmc2_1$ phase and the phase fraction of the $R3c$ phase. (b) Lattice parameters of the $R3c$ phase. (c) The global amplitudes of the main modes in both the $Pmc2_1$ and $R3c$ phases, changing as a function of $LiTaO_3$ content.

previously reported (Khan *et al.*, 2012). Note that due to overlapping, peak intensities are easily influenced by cross-talk. Furthermore, the BVS calculation indicates that Li^+ would prefer to move away from the Ag site to an interstitial site (Alonso *et al.*, 2000; Brant *et al.*, 2012). Therefore, the reliability factors of the refinement on ANLT9 are not as good as those for the lower-level $LiTaO_3$ doped samples (Table S3). Due to the detection of a secondary phase, a deviation in x from 9% for $LiTaO_3$ is probably expected. The refinement results reveal that the molar fraction of this secondary phase is around 2.5%, suggesting that the dopant level of $LiTaO_3$ is around 6.5%. Application of the modified composition did indeed improve the reliability factors (R_p changes from 0.0268 to 0.0260). Therefore, in the following we assume a $LiTaO_3$ content of 6.5% for ANLT9 in order to guide the reader's understanding of the structural evolution as a function of $LiTaO_3$ content. Details of the refined atomic positions of the ANLT100x system are shown in the supporting information (Tables S4–S9).

Fig. 6 shows the structural evolution of the ANLT100x materials as a function of $LiTaO_3$ content. In the $Pmc2_1$ single-phase region, *i.e.* $x < 0.053$, the unit-cell parameters (a, b and c) decrease gradually with respect to the x value [Fig. 6(a)]. This shrinkage of the unit cell is possibly due to the intro-duction of Li^+, whose ionic radius is 92 pm compared with the 128 pm radius of Ag^+ (Shannon, 1976). When the $R3c$ phase appears (at $x = 0.053$), the a, b and c values for the ortho-

rhombic phase exhibit a slight increase. In the two-phase region, *i.e.* $x \geq 0.053$, with further doping the lattice parameter a increases, whereas b and c decrease. On the other hand, the fraction of the $R3c$ phase increases from 12.1 to 53% for $0.053 \leq x \leq 0.06$. For the $R3c$ phase, both a and c are reduced with increasing x [Fig. 6(b)]. The variation in the unit-cell para-meters of both the $Pmc2_1$ and $R3c$ structures cannot simply be explained by the ionic radii; it is probably linked to octahedral rotation and interaction between the two phases.

Fig. 6(c) shows the global amplitude (A_τ) of the main modes changing as a function of $LiTaO_3$ content for both the $Pmc2_1$ and $R3c$ phases. Larger A_τ values imply larger atomic displacements and a more highly distorted structure. In the $Pmc2_1$ phase, referring to the mode decomposition in pure AN, the four critical modes can be divided into ionic displace-ments (FE Γ4− and AFE Λ3) and octahedral rotations (H2 and T4+). The amplitudes of the H2 and Λ3 modes decrease upon Li^+ doping. However, the slope has an inflexion point at $x = 0.053$ and descends rapidly upon further Li^+ doping. The amplitude of the FE Γ4− mode, on the other hand, displays the opposite trend to that of the AFE Λ3 mode. It is note-worthy that the deviation of the Γ4− mode's amplitude becomes quite large when $x \geq 0.053$, indicating that the variation of this parameter has less impact on the refinement results.

In Section 2.1 we described the distorted structure induced by the largest-amplitude single modes, and also found that the overall octahedral tilting pattern is induced by a combination of T4+ and H2 modes. Instead of the related oxygen displacements, the tilting angles can also be used to reflect the
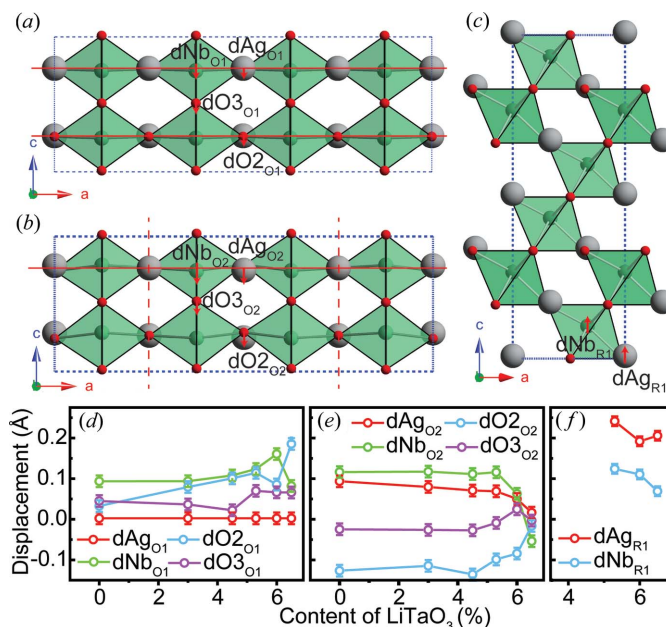
Figure 7
The distorted structure induced by (*a*) the T4+ mode for the *Pmc*2₁ phase viewed along the b_p axis, (*b*) the H2 mode for the *Pmc*2₁ phase viewed along the c_p axis and (*c*) the R4+ mode for the *R*3*c* phase viewed along the c_p axis. (*d*) The LiTaO₃ content-dependent rotation angles.

degrees of distortion for these octahedral rotation modes. As shown in Fig. 7(*a*), the structure induced by the T4+ mode can be visually expressed by the tilting angles between the two adjacent NbO₆ octahedra viewed along either [100]ₚ or [010]ₚ. Here, Ψ_{O1} and Ψ_{O2} (subscript O denotes the orthorhombic phase) are used to illustrate the tilt angles. If there is no octahedral distortion, $\Psi_{O1} = \Psi_{O2}$. The H2 mode is associated with the in- or antiphase rotation around [001]ₚ and Ψ_{O3} is used to characterize the tilting angle for this mode [Fig. 7(*b*)].

In the *R*3*c* phase, the R4+ mode denotes $a^-a^-a^-$ octahedral tilting, and therefore the tilt angle along any ⟨100⟩ₚ direction, Ψ_{R1} (subscript R denotes the rhombohedral phase), is used to describe this distorted structure [Fig. 7(*c*)]. Fig. 7(*d*) shows the quantitative analysis of these rotation angles. For Ψ_{O1} and Ψ_{O2}, they are almost equivalent when $x \leq 0.053$, and both increase slightly as the doping level increases. When $x \geq 0.053$, Ψ_{O1} and Ψ_{O2} behave differently: Ψ_{O1} increases, whereas Ψ_{O2} decreases. This suggests that the octahedral distortion is accompanied by the appearance of the *R*3*c* phase. Furthermore, the decrease in Ψ_{O2} also explains the increase in the unit-cell parameter *a* for $x \geq 0.053$. The tilt angle Ψ_{R1} increases with increases in the heavily underbonded Li⁺ dopants. For the H2 mode, Ψ_{O3} decreases slightly before the appearance of the *R*3*c* phase and then sharply when the *R*3*c* phase dominates the samples. This behaviour is very similar to that of primary modes that vary as a function of temperature in other materials (Khalyavin *et al.*, 2014; Faik *et al.*, 2012; Gómez-Pérez *et al.*, 2016). Therefore, the destabilization of the H2 mode is very important to this composition-driven phase transition in the ANLT100*x* system.

Note that the sudden drop in Ψ_{O3} is deduced by the change in the degree of ordering of $a^0a^0c^+/a^0a^0c^-$ octahedral tilting. This is probably due to the fact that the rotation around [001]ₚ creates differing periodicities or is totally disordered (Khan *et al.*, 2012; Wang *et al.*, 2011; Guo *et al.*, 2011; Liu *et al.*, 2012; Bellaiche & Íñiguez, 2013; Prosandeev *et al.*, 2013), *i.e.* the associated modulation wavevector moves along the H line in

Figure 8
The distorted structure induced by (*a*) the Γ4− mode and (*b*) the Λ3 mode for the *Pmc*2₁ phase, viewed along the *b* axis. The red solid lines indicate the *z* coordinates for the undistorted structure, the vertical dashed red lines in panel (*b*) show the boundaries of the two-layer octahedral units within which the dipole moments share the same direction, and the red arrows denote the displacements of the respective ions. (*c*) The distorted structure induced by the Γ4− mode for the *R*3*c* phase, viewed along the *b* axis. (*d*), (*e*), (*f*) The ionic displacements induced by (*d*) the Γ4− mode, (*e*) the Λ3 mode in the *Pmc*2₁ phase and (*f*) the Γ4− mode in the *R*3*c* phase as a function of LiTaO₃ content.

the first Brillouin zone of the parent *Ammm* structure. In the Li-doped AgNbO₃ material system (Khan *et al.*, 2012, 2010), electron diffraction patterns show $\mathbf{G}_p \pm [1/2\ 1/2\ 1/3]_p^*$ satellite reflections, which in turn indicate a movement to the zone boundary (T point) of the H2 mode. Finally, the combination of the T2+ ($a^0a^0c^-$) and T4+ modes induces the $a^-a^-a^-$ octahedral tilting observed in the *R*3*c* phase, and therefore the variation in the H2 mode locally builds an intermediate structure between the *Pmc*2₁ and *R*3*c* phases.

As mentioned above, the Γ4− mode is responsible for ferroelectricity in both the *Pmc*2₁ and *R*3*c* phases, while the Λ3 mode is associated with antiferroelectricity for the *Pmc*2₁ phase. Note that the Λ3 mode can be regarded as a secondary mode induced by primary H2 and T4+ modes, and its composition-dependent amplitude follows the same trend as the H2 mode, suggesting an improper AFE nature of AN (Bellaiche & Íñiguez, 2013).

In order to analyse the (anti)ferroelectricity further, the ionic displacements associated with the different modes are extracted and plotted as a function of composition in Fig. 8. Although some atomic displacements along the *b* axis are involved in both Γ4− and Λ3 modes in the *Pmc*2₁ phase (Table S2), the refined values are quite small. Furthermore, because the (anti)parallel dipole moments are aligned along the *c* axis, only displacements from the *z* coordinates are considered. For the Γ4− mode in the *Pmc*2₁ phase [Fig. 8(*a*)], $dO2_{O1}$ (displacement of the apical oxygen), $dO3_{O1}$

(displacement of the equatorial oxygens), $d\text{Ag}_{\text{O1}}$ (Ag/Li) and $d\text{Nb}_{\text{O1}}$ (Nb/Ta) denote the ionic displacements along −**c** from the undistorted position (subscripts O and 1 indicate the orthorhombic phase and the Γ4− mode, respectively). Fig. 8(b) gives a schematic description of the ionic displacements associated with the Λ3 mode. As the dipole moments exhibit antiparallel alignment with the same amplitude, only atoms involved in one unit are extracted (subscript 2 denotes the Λ3 mode). In this case, only the displacements of Ag/Li2 ($d\text{Ag}_{\text{O2}}$), Nb/Ta1 ($d\text{Nb}_{\text{O2}}$), apical oxygen ($d\text{O2}_{\text{O2}}$) and equatorial oxygen ($d\text{O3}_{\text{O2}}$) are extracted. Similarly, $d\text{Ag}_{\text{R1}}$ (Ag/Li) and $d\text{Nb}_{\text{R1}}$ (Nb/Ta) are used to describe the ferroelectricity in the R3c phase [Fig. 8(c)]. Note that in the R3c phase, the z coordinate of the oxygen is fixed to zero, therefore cationic shifts are enough to describe the spontaneous polarization.

It is interesting that, even though the amplitude of the Γ4− mode in the $Pmc2_1$ phase exhibits a systematic increase as a function of x, the change in both $d\text{O2}_{\text{O1}}$ and $d\text{Nb}_{\text{O1}}$ indicates that spontaneous polarization does not follow the same trend, especially when $x \geq 0.053$ [Fig. 8(d)]. The zone-centre mode is very hard to calculate accurately via powder diffraction. The large deviations suggest that the structure models based on both $Pmc2_1$ and Pbcm reproduce the experimental pattern reasonably well. By contrast, the refined values of $d\text{O2}_{\text{O2}}$, $d\text{O3}_{\text{O2}}$, $d\text{Ag}_{\text{O2}}$ and $d\text{Nb}_{\text{O2}}$ involved in the Λ3 mode change systematically as a function of LiTaO3 content [Fig. 8(e)]. Before introducing the LiTaO3, the cations and anions are displaced in opposite directions, i.e. $d\text{O2}_{\text{O2}}$ and $d\text{O3}_{\text{O2}} < 0$, and $d\text{Ag}_{\text{O2}}$ and $d\text{Nb}_{\text{O2}} > 0$, leading to a strong spontaneous polarization within any one two-octahedral-layer unit. With increasing x, the displacements of the anions and cations begin to converge, until a sudden change occurs at $x \simeq 0.053$. This behaviour suggests that the dipole moment in each sublattice becomes smaller, i.e. the antiferroelectricity is weakening. For $x \geq 0.053$, the R3c phase emerges and its fractional content rises with further increase in x, whereas the diminishing $Pmc2_1$ phase is simultaneously accompanied by a weakening antiferroelectricity. As a consequence, the ferroic properties are expected to be dominated by the R3c phase in this composition region. As shown in Fig. 8(f), for the sample with the largest R3c phase fraction ($x \geq 0.06$), $d\text{Ag}_{\text{R1}}$ remains unchanged while $d\text{Nb}_{\text{R1}}$ shows a slight decrease.

2.3. Electrical properties

Fig. 9 shows the temperature-dependent dielectric spectra of ANLT100x bulk ceramics. That for pure AN contains three evident dielectric constant peaks, T_{I} (∼70°C), T_{II} (∼270°C) and T_{III} (∼350°C), in the measured temperature range from −150 to 480°C, consistent with the previously reported experimental results (Fu et al., 2007). In this temperature range, AN is reported to contain six phases: M1, M2, M3, O1, O2 and T. The M1, M2 and M3 phases have orthorhombic structures (the M label denotes the monoclinic distortion of the primitive unit cell) and all of them exhibit antiferroelectricity (Ratuszna et al., 2003; Kania, 2001). The peaks at the ∼T_{I} and T_{II} points are assigned to the M1–M2 and

M2–M3 phase transitions, respectively. The sharp peak at the T_{III} point is attributed to the phase transition between the AFE M3 phase and a paraelectric O1 phase with a space-group symmetry of Cmcm. Previously, the average structures of the M1, M2 and M3 phases were all assigned to the same Pbcm space-group symmetry. The phase transitions between the three phases were interpreted as cation displacements (Levin et al., 2009, 2010; Krayzman & Levin, 2010). The broad T_{II} peak was proved to be the result of Nb5+ displacement dynamics, while the origin of the frequency-dependent T_{I} peak is still under debate (Levin et al., 2009). Recently, the T_{I}-related peak was explained as being due to the disappearance of weak ferroelectricity within the recently proposed polar $Pmc2_1$ phase, i.e. the softening of the above-mentioned Γ4− mode (Manish et al., 2015).

The temperature-dependent dielectric spectra of ANLT3 and ANLT4.5 [Figs. 9(b) and 9(c)] are quite similar to pure AN, again accompanied by three dielectric peaks at T_{I}, T_{II} and T_{III}. Interestingly, the T_{I} peak shifts gradually towards low temperature with increasing concentration of LiTaO3 and, at the same time, the refined Γ4− mode at room temperature becomes unstable. Furthermore, the increase in LiTaO3 content also shifts the T_{II} peak to lower temperature with a larger dielectric constant. As mentioned above, the M3–M2 phase transition has been associated with differing degrees of order for the Nb ions. Referring to the results of Levin et al. (2009), ordered octahedral tilting will promote the long-range order of the Nb displacements. From our experimental data, the H2 mode drops slightly with increasing x ($x \leq 0.045$), which possibly suggests that the octahedral tilting becomes disordered. Therefore, this order–disorder transition can be activated at a lower thermal energy with increasing dopant concentration, thereby moving the transition point towards lower temperature. With further increases in x, an additional dielectric peak T_{U} is first observed around 140°C in ANLT5.3 and becomes dominant in the ANLT6 and ANLT9 spectra.
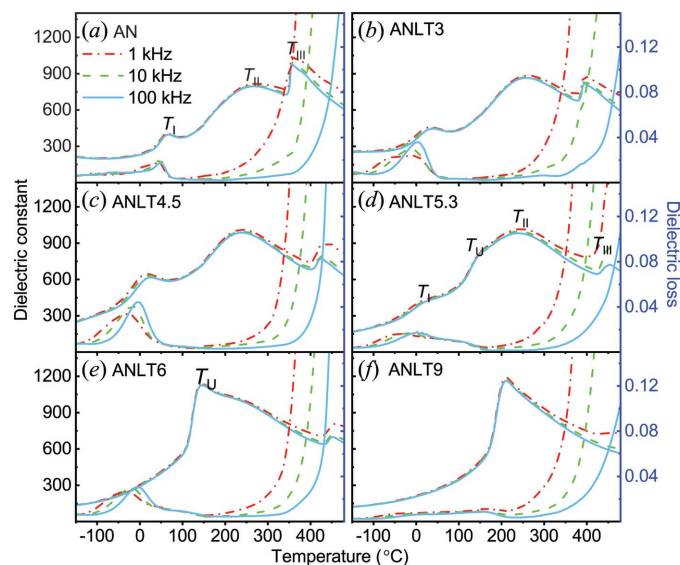
Figure 9
Temperature-dependent dielectric spectra for (a) AN, (b) ANLT3, (c) ANLT4.5, (d) ANLT5.3, (e) ANLT6 and (f) ANLT9 bulk ceramics.
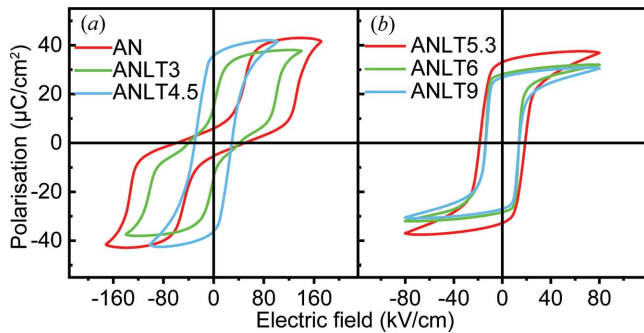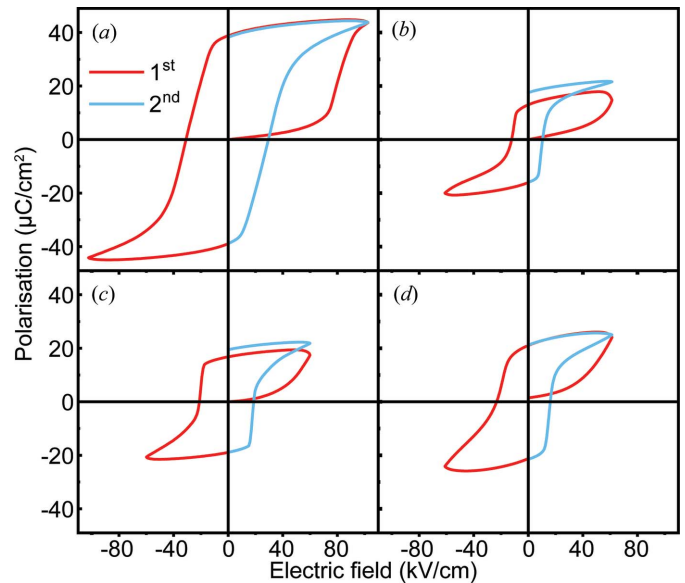
Figure 10
Room-temperature *P-E* hysteresis loops for (*a*) AN, ANLT3 and ANLT4.5, and (*b*) ANLT5.3, ANLT6 and ANLT9 bulk ceramics measured at 1 Hz.

After the appearance of the T_U peak, the T_I, T_{II} and T_{III} related dielectric peaks become systematically more blurred with increasing *x* and almost unobservable in the dielectric constant spectra of ANLT9, although there are still traces in the dielectric loss spectra. The appearance of the T_U peak is quite consistent with the results in the Li-doped $AgNbO_3$ material system and this dielectric anomaly is clearly related to the phase transition between the *R3c* FE and AFE phases (Fu *et al.*, 2011*b*). Therefore, the variation in the T_U peak as a function of *x* can be well explained by the growth in the phase fraction of the *R3c* phase in the ANLT100*x* material system.

Fig. 10 shows the polarization–electric field (*P-E*) hysteresis loops of ANLT100*x* bulk ceramics. Pure AN presents a double *P-E* hysteresis loop with an induced polarization of 41 μC cm^{-2} under an applied field of 175 kV cm^{-1}. The critical *E* field (E_F) to induce the FE state at 1 Hz is around 125 kV cm$^-$ and the non-zero remnant polarization (P_r) is around 6 μC cm^{-2} after withdrawal of the *E* field. These results are almost identical to those reported earlier by Fu *et al.* (2007). The observed *P-E* hysteresis loop confirms the AFE nature of AN, accompanied by weak ferroelectricity. Similar to pure AN, a double *P-E* hysteresis loop is also obtained for ANLT3 [Fig. 10(*a*)] but E_F decreases to 100 kV cm^{-1} and non-zero P_r to ~14 μC cm^{-2}. The decrease in the critical field indicates the decreasing energy barrier between the AFE and the induced FE state with increasing *x*. This is consistent with the gradual decrease in the mode amplitude of the Λ3 mode as a function of *x*. The AFE feature, *i.e.* the double *P-E* hysteresis loop, disappears experimentally at a composition of ANLT4.5. Instead, a highly saturated single hysteresis loop is observed with a maximum polarization (P_m) ≃ 42 μC cm^{-2} and a P_r ≃ 36 μC cm^{-2} when a cycled *E* field of 100 kV cm^{-1} is applied. With a further increase in *x*, the ANLT100*x* samples exhibit typical FE features and both P_m and P_r decrease slightly. For samples showing two-phase coexistence (*x* ≥ 0.053), the FE properties seem to be determined by the Γ4− mode in the *R3c* phase. Intriguingly, with a further increase in the nominal *x* value, the amplitude of the Γ4− mode, *i.e.* the spontaneous polarization, decreases.

The NPD pattern and temperature-dependent dielectric spectrum of ANLT4.5 suggest that the pristine sample contains a single AFE phase, but its *P-E* hysteresis loop shows

Figure 11
P-E loops for (*a*) ANLT4.5, (*b*) ANLT5.3, (*c*) ANLT6 and (*d*) ANLT9 measured at 1 Hz in the first cycle (red) and second semi-cycle (blue).

an FE nature [Fig. 10(*a*)]. In order to understand the AFE/FE behaviour observed in the ANLT100*x* system, the *P-E* hysteresis loops measured in the first and second cycles are displayed in Fig. 11. It is evident that the polarization of ANLT4.5 increases abruptly after the first quarter *E* field cycle, and after that the *P-E* loop behaves like that observed in a classical FE material. This is very similar to the irreversible *E* field-induced AFE–FE phase transition observed in PbZrO₃-based AFE materials (Lu *et al.*, 2017; Guo & Tan, 2015). Furthermore, the E_F for ANLT4.5 is around 90 kV cm^{-1}, presenting a further decrease compared with that observed for ANLT3. For *x* ≥ 0.053, the steep increase in the polarization is hardly observed, and instead the polarization rises gradually over the first quarter cycle. After the first quarter cycle (same amplitude), the P_r values of ANLT5.3, ANLT6 and ANLT9 are around 13, 17 and 20 μC cm^{-2}, respectively. Furthermore, after the second cycle, the P_r values of ANLT5.3 and ANLT6 show a slight increase, while that of ANLT9 remains almost constant.

The evolution of the measured electrical properties in the ANLT100*x* series can be well understood from a structural viewpoint and is summarized in Fig. 12. For the pure AN sample, the distorted structure is dominated by two octahedral tilting modes (T4+ and H2), but the secondary Λ3 AFE mode still has a relatively large mode amplitude. Thus, a characteristic double *P-E* hysteresis loop is obtained. Upon increasing the content of LiTaO₃, the H2 mode, *i.e.* the $a^0a^0c^-/a^0a^0c^+$ octahedral tilting mode, becomes destabilized due to the heavily underbonded Li⁺ ions and the associated AFE mode is simultaneously damped. The antiferroelectricity hence becomes weak and a lower *E* field is able to trigger an AFE–FE phase transition. Upon further increasing *x* to 0.053, the rhombohedral *R3c* phase appears and, at this stage, the samples contain both $Pmc2_1$ and *R3c* phases. The coexistence of the two phases implies a relatively flat energy landscape
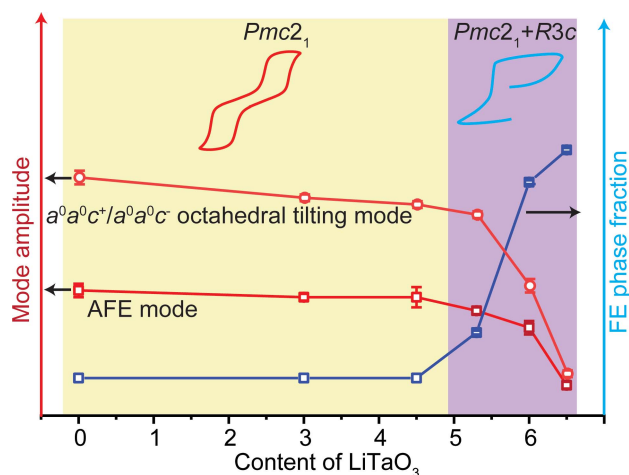
Figure 12
A schematic drawing that reflects the structure–property relationships present in the ANLT100x material system in the form of symmetry modes, phases and electrical properties.

connecting the $Pmc2_1$ and $R3c$ structures. Therefore, as shown by the different P-E behaviour measured in the first and second cycles, although the virgin state of the sample has an AFE nature, the FE state will be stabilized after applying an E field. As the $R3c$ phase fraction increases, the samples' antiferroelectricity is further weakened. After applying a first-cycle E field with the same amplitude, ANLT9 exhibits the largest remnant polarization.

3. Conclusions

A symmetry-mode decomposition of AgNbO$_3$ identifies the differences between the $Pbcm$ and $Pmc2_1$ structures. Both distorted structures share three main modes (T4+, H2 and Λ3) with large amplitudes. The only difference between the $Pbcm$ and $Pmc2_1$ structures is the 'softening' of the zone-centre $\Gamma4-$ mode, which lowers the non-polar $Pbcm$ symmetry structure into $Pmc2_1$ symmetry and is regarded as the origin of the weak ferroelectricity observed in AgNbO$_3$. Upon doping LiTaO$_3$ into AN, the H2 mode associated with in- or antiphase octahedral tilting around $[001]_p$ gradually becomes destabilized, while another octahedral rotation mode (T4+, $a^-a^-c^0$ tilting) shows no such significant variation. The secondary Λ3 mode (induced by the two octahedral rotation modes) controls the antiferroelectric behaviour observed in the samples, which is then damped as a result of the H2 mode destabilization. With further LiTaO$_3$ doping, another $R3c$ phase appears and the samples contain two phases, suggesting a low energy barrier between the $Pmc2_1$ and $R3c$ structures. Considering the octahedral tilting modes in both phases, we postulate that the disappearance of the H2 mode as a function of increasing x is the main force driving the structural evolution of the ANLT100x material system. More importantly, through symmetry-mode analysis this work provides a detailed physical picture of the phase transition in the ANLT100x system and builds an intuitive connection to the obtained electrical properties. We believe that this work provides

insight into how to tune the electrical properties by controlling the amplitudes of the relative modes in these antiferroelectric and ferroelectric materials. It also introduces a novel approach to structure refinement that provides information on the hidden structural correlations for a better understanding of the materials' physical properties.

References

Alonso, J. A., Sanz, J., Santamaría, J., León, C., Várez, A. & Fernández-Díaz, M. T. (2000). *Angew. Chem. Int. Ed.* **39**, 619–621.
Bellaiche, L. & Íñiguez, J. (2013). *Phys. Rev. B*, **88**, 014104.
Bellaiche, L. & Vanderbilt, D. (1999). *Phys. Rev. Lett.* **83**, 1347–1350.
Brant, W. R., Schmid, S., Kuhn, A., Hester, J., Avdeev, M., Sale, M. & Gu, Q. (2012). *ChemPhysChem*, **13**, 2293–2296.
Brown, I. D. (1981). *Structure and Bonding in Crystals*, Vol. 2, edited by M. O'Keeffe & A. Navrotsky, pp. 1–13. New York: Academic Press.
Campbell, B. J., Stokes, H. T., Tanner, D. E. & Hatch, D. M. (2006). *J. Appl. Cryst.* **39**, 607–614.
Damjanovic, D. (1998). *Rep. Prog. Phys.* **61**, 1267–1324.
Dove, M. T. (1997). *Am. Mineral.* **82**, 213–244.
Faik, A., Orobengoa, D., Iturbe-Zabalo, E. & Igartua, J. M. (2012). *J. Solid State Chem.* **192**, 273–283.
Fu, D., Arioka, T., Taniguchi, H., Taniyama, T. & Itoh, M. (2011a). *Appl. Phys. Lett.* **99**, 012904.
Fu, D., Endo, M., Taniguchi, H., Taniyama, T. & Itoh, M. (2007). *Appl. Phys. Lett.* **90**, 252907.
Fu, D., Endo, M., Taniguchi, H., Taniyama, T., Itoh, M. & Koshihara, S. (2011b). *J. Phys. Condens. Matter*, **23**, 075901.
Fu, D., Endo, M., Taniguchi, H., Taniyama, T., Koshihara, S. & Itoh, M. (2008). *Appl. Phys. Lett.* **92**, 172905.
Fu, D., Itoh, M. & Koshihara, S. (2009). *J. Appl. Phys.* **106**, 104104.
Glazer, A. M. (1975). *Acta Cryst.* A**31**, 756–762.
Gómez-Pérez, A., Hoelzel, M., Muñoz-Noval, A., García-Alvarado, F. & Amador, U. (2016). *Inorg. Chem.* **55**, 12766–12774.
Guo, H. & Tan, X. (2015). *Phys. Rev. B*, **91**, 144104.
Guo, R., Cross, L. E., Park, S. E., Noheda, B., Cox, D. E. & Shirane, G. (2000). *Phys. Rev. Lett.* **84**, 5423–5426.
Guo, Y., Liu, Y., Withers, R. L., Brink, F. & Chen, H. (2011). *Chem. Mater.* **23**, 219–228.
Haertling, G. H. (1999). *J. Am. Ceram. Soc.* **82**, 797–818.
Hao, X., Zhai, J. & Yao, X. (2009). *J. Am. Ceram. Soc.* **92**, 1133–1135.
Kania, A. (2001). *J. Phys. D Appl. Phys.* **34**, 1447–1455.
Khalyavin, D. D., Salak, A. N., Olekhnovich, N. M., Pushkarev, A. V., Radyush, Y. V., Manuel, P., Raevski, I. P., Zheludkevich, M. L. & Ferreira, M. G. S. (2014). *Phys. Rev. B*, **89**, 174414.
Khan, H. U., Sterianou, I., Han, Y., Pokorny, J. & Reaney, I. M. (2010). *J. Appl. Phys.* **108**, 064117.

Khan, H. U., Sterianou, I., Miao, S., Pokorny, J. & Reaney, I. M. (2012). *J. Appl. Phys.* **111**, 024107.

Krayzman, V. & Levin, I. (2010). *J. Phys. Condens. Matter*, **22**, 404201.

Levin, I., Krayzman, V., Woicik, J. C., Karapetrova, J., Proffen, T., Tucker, M. G. & Reaney, I. M. (2009). *Phys. Rev. B*, **79**, 104113.

Levin, I., Woicik, J. C., Llobet, A., Tucker, M. G., Krayzman, V., Pokorny, J. & Reaney, I. M. (2010). *Chem. Mater.* **22**, 4987–4995.

Liu, Y., Norén, L., Studer, A. J., Withers, R. L., Guo, Y., Li, Y., Yang, H. & Wang, J. (2012). *J. Solid State Chem.* **187**, 309–315.

Liu, Z., Chen, X., Peng, W., Xu, C., Dong, X., Cao, F. & Wang, G. (2015). *Appl. Phys. Lett.* **106**, 262901.

Lu, T., Studer, A. J., Yu, D., Withers, R. L., Feng, Y., Chen, H., Islam, S. S., Xu, Z. & Liu, Y. (2017). *Phys. Rev. B*, **96**, 214108.

Manish, K. N., Prasad, K. G., Saket, A., Rayaprol, S. & Siruguri, V. (2015). *J. Phys. D Appl. Phys.* **48**, 215303.

Mirshekarloo, M. S., Yao, K. & Sritharan, T. (2010). *Appl. Phys. Lett.* **97**, 142902.

Park, S.-E. & Shrout, T. R. (1997). *J. Appl. Phys.* **82**, 1804–1811.

Perez-Mato, J. M., Orobengoa, D. & Aroyo, M. I. (2010). *Acta Cryst.* A**66**, 558–590.

Prosandeev, S., Wang, D., Ren, W., Íñiguez, J. & Bellaiche, L. (2013). *Adv. Funct. Mater.* **23**, 234–240.

Ratuszna, A., Pawluk, J. & Kania, A. (2003). *Phase Transit.* **76**, 611–620.

Rodríguez-Carvajal, J. (1993). *Physica B*, **192**, 55–69.

Saito, Y., Takao, H., Tani, T., Nonoyama, T., Takatori, K., Homma, T., Nagaya, T. & Nakamura, M. (2004). *Nature*, **432**, 84–87.

Sciau, P., Kania, A., Dkhil, B., Suard, E. & Ratuszna, A. (2004). *J. Phys. Condens. Matter*, **16**, 2795–2810.

Setter, N., Damjanovic, D., Eng, L., Fox, G., Gevorgian, S., Hong, S., Kingon, A., Kohlstedt, H., Park, N. Y., Stephenson, G. B., Stolitchnov, I., Taganstev, A. K., Taylor, D. V., Yamada, T. & Streiffer, S. (2006). *J. Appl. Phys.* **100**, 051606.

Shannon, R. D. (1976). *Acta Cryst.* A**32**, 751–767.

Shrout, T. R. & Zhang, S. J. (2007). *J. Electroceram.* **19**, 113–126.

Stokes, H. T., Hatch, D. M. & Wells, J. D. (1991). *Phys. Rev. B*, **43**, 11010–11018.

Tian, Y., Jin, L., Zhang, H., Xu, Z., Wei, X., Politova, E. D., Stefanovich, S. Y., Tarakina, N. V., Abrahams, I. & Yan, H. (2016). *J. Mater. Chem. A*, **4**, 17279–17287.

Tian, Y., Jin, L., Zhang, H., Xu, Z., Wei, X., Viola, G., Abrahams, I. & Yan, H. (2017). *J. Mater. Chem. A*, **5**, 17525–17531.

Wang, J., Liu, Y., Withers, R. L., Studer, A., Li, Q., Norén, L. & Guo, Y. (2011). *J. Appl. Phys.* **110**, 084114.

Yashima, M., Matsuyama, S., Sano, R., Itoh, M., Tsuda, K. & Fu, D. S. (2011). *Chem. Mater.* **23**, 1643–1645.

Zhao, L., Gao, J., Liu, Q., Zhang, S. & Li, J.-F. (2018). *ACS Appl. Mater. Interfaces*, **10**, 819–826.

Zhao, L., Liu, Q., Gao, J., Zhang, S. & Li, J. (2017). *Adv. Mater.* **29**, 1701824.

Zhao, L., Liu, Q., Zhang, S. & Li, J.-F. (2016). *J. Mater. Chem. C.* **4**, 8380–8384.